TM 82117

REMOTE SENSING OF PRECIPITABLE WATER OVER THE OCEANS FROM NIMBUS-7 MICROWAVE MEASUREMENTS

C. Prabhakara

H. D. Chang*

A. T. C. Chang

April 1981

GODDARD SPACE FLIGHT CENTER
Greenbelt, Maryland

* Computer Sciences Corporation, Silver Spring, Md.

REMOTE SENSING OF PRECIPITABLE WATER OVER THE OCEANS FROM NIMBUS-7 MICROWAVE MEASUREMENTS

C. Prabhakara
H. D. Chang*
A. T. C. Chang

ABSTRACT

Nimbus-7 Scanning Multichannel Microwave Radiometer (SMMR) brightness temperature measurements in the 21 and 18 GHz channels are used to sense the precipitable water in the atmosphere over oceans. The difference in the brightness temperature ($T_{21}-T_{18}$), both in the horizontal and vertical polarization, is found to be essentially a function of the precipitable water in the atmosphere. An equation, based on the physical considerations of the radiative transfer in the microwave region, is developed to relate the precipitable water to ($T_{21}-T_{18}$). It is shown from theoretical calculations that the signal ($T_{21}-T_{18}$) does not suffer severely from the noise introduced by variations in the sea surface temperature, surface winds, and liquid water content in non-raining clouds. The rms deviation between the estimated precipitable water from SMMR data and that given by the closely coincident ship radiosondes is about 0.25 g/cm^2.

Global maps of precipitable water over oceans derived from SMMR data reveal several salient features associated with ocean currents and the large scale general circulation in the atmosphere.

* Computer Sciences Corporation, Silver Spring, Md.

REMOTE SENSING OF PRECIPITABLE WATER OVER THE OCEANS FROM NIMBUS-7 MICROWAVE MEASUREMENTS

INTRODUCTION

Water vapor in the atmosphere is an important constituent because it plays a significant role in the absorption and emission of radiative energy, and in the development of fog, clouds, and precipitation. Remote sensing of this constituent on a global basis can be of aid in the understanding and prediction of weather and climate processes. Because of the low vertical resolution (~3 km) obtainable with present passive remote sensing techniques, the accuracy of the derived vertical profile of water vapor is poor (Conrath, 1969; Smith and Woolf, 1976). However, the vertically integrated water vapor amount (precipitable water), particularly over water bodies, can be determined fairly accurately.

Precipitable water in the atmosphere over the oceans is a useful parameter which indicates the dynamic state of the atmospheric boundary layer. When low level convergence is present in the atmosphere, a deep convective layer is formed resulting in a relatively large amount of precipitable water. On the other hand, when stable conditions, prevail, such as those associated with low level inversions, a dry layer above the inversion is formed and the precipitable water in the atmosphere is consequently reduced. In a recent study using the Nimbus-4 Infrared Interferometer Spectral measurements Prabhakara et al., (1979) have derived precipitable water over the global oceans for each season, and thereby inferred the structure of the atmospheric boundary layer.

In the remote sensing of sea surface temperatures from infrared window radiance measurements, it is necessary to apply a correction for atmospheric water vapor absorption. Satellite sensing of the precipitable water can thus help improve the accuracy of the sea surface temperature measurement.

Remote sensing of the precipitable water over the global oceans utilizing microwave measurements from Nimbus-5 and -6 has been demonstrated, amongst other by Staelin et al., (1976), Chang and Wilheit (1979), and Grody et al., (1980). The capability of microwave remote sensing through non-precipitating clouds is particularly valuable in getting global information on time scale of about a week or less. The retrieval techniques used in thsee studies depend either on multiple regression, or on an approximation to the radiative transfer formalism. These methods have yielded an rms error in the estimated precipitable water of about 0.45 $g/_{cm}{}^2$.

The Nimbus-7 SMMR has two channels closely spaced in the spectrum, at 18 and 21 GHz (see Fig. 2), located on one side of the weak water vapor line centered at 22.235 GHz. The difference between the brightness temperature in these two channels yields a measure of the absorption strength of this weak water vapor line. Since the absorption strength of a weak line is proportional to the amount of absorbing gas (Plass, 1960), we can relate the brightness temperature difference to the precipitable water in the atmosphere. The retrieval technique developed in this study differs from the previous ones in this respect. This method is applied to the Nimbus -7 SMMR observations made over ship stations (see Table 1) that had radiosonde measurements. The satellite sensed precipitable water agrees with that given by the radiosonde measurements to within an rms error of 0.25 $g/_{cm}{}^2$.

Table 1

Comparison of remotely sensed precipitable water vs. ship radiosonde measurements

CASE NO.	DATE	LAT	LONG	$(T_{21}-T_{18})^V$ °K	w(gm/cm²) SMMR	w(gm/cm²) RADIO SONDE	Δ W
1	10/25/78	36°N	22.9°W	31.4	3.60	3.29	0.31
2	10/25/78	52.8°N	35.5°W	30.6	3.48	3.43	0.05
3	10/25/78	29°N	135°E	31.5	3.48	3.34	0.14
4	10/26/78	50°N	145°W	15.9	1.17	1.04	0.13

Table 1 (cont.)

CASE NO.	DATE	LAT	LONG	$(T_{21}^{\bullet} - T_{18})V$ $^{\circ}K$	w(gm/cm^2) SMMR	w(gm/cm^2) RADIO SONDE	Δ W
5	10/26/78	52.8°N	35.5°W	24.9	2.58	3.02	-0.44
6	10/26/78	36°N	27.8°W	30.1	3.39	3.43	-0.04
7	10/28/78	66°N	2°E	10.1	0.54	0.67	-0.13
8	10/31/78	52.8°N	35.5°W	11.8	0.76	0.84	-0.08
9	11/05/78	50°N	145°W	21.4	2.07	2.34	-0.27
10	11/05/78	38.8°N	134.7°E	14.8	1.15	1.36	-0.21
11	11/06/78	66°N	2°E	10.2	0.56	0.55	0.01
12	02/15/79	47°N	17°W	15.9	1.3	1.15	0.15
13	02/15/79	66°N	2°E	11.5	0.74	0.7	0.04
14	02/15/79	50°N	145°W	10.8	0.63	0.62	0.01
15	02/15/79	57°N	20°W	12.3	0.82	1.11	-0.29
16	02/17/79	57°N	20°W	22.2	2.18	1.94	0.24
17	02/17/79	46.5°S	20.3°E	18.5	1.65	1.15	0.5
18	02/19/79	5.5°S	65.3°E	37.5	4.66	4.69	-0.03
19	02/19/79	50°N	145°W	16.0	1.31	1.3	0.01
20	02/21/79	11.8°S	65.2°E	38.2	4.6	4.84	-0.24
21	02/23/79	57°N	20°W	18.4	1.64	1.37	0.27
22	02/23/79	37°S	155.3°E	22.6	2.24	2.15	0.09
23	02/23/79	38.2°S	24.1°E	24.5	2.53	2.37	0.16
24	02/23/79	9.1°N	110.1°E	31.7	3.65	3.86	-0.21
25	02/25/79	4.9°N	30°W	34.3	4.09	4.7	-0.61
26	02/25/79	47°N	17°W	19.3	1.76	1.58	0.18
27	02/25/78	23°S	66.3°E	39.4	5.02	4.88	0.14
28	02/25/79	32.4°S	37.1°E	31.3	3.6	2.89	0.71

• After removal of 8.5°K systematic bias.

THEORETICAL BACKGROUND:

In the microwave region, spanning the SMMR frequencies from about 6 to 37 GHz, the principal absorber in the atmosphere is water vapor. In addition liquid water droplets contained in non-raining clouds, smaller than ~100 μm in radius, produce some absorption which increases approximately as the square of the frequency. This Rayleigh approximation which holds well for droplets smaller than ~100 μm starts to break down for large rain drops and Mie scattering gains importance (Gunn and East, 1954). The wind at the surface of the ocean changes the roughness of the water and thereby the surface emissivity, and, in addition, at wind speeds above about 7 m/sec white caps are formed which markedly affect the sea surface emissivity. These physical effects have been discussed in the earlier studies of Wilheit et al., (1975), Wilheit (1978), Chang and Wilheit (1979), and Staelin et al., (1976). In this study an attempt is made to take advantage of the known physics and arrive at an algorithm that improves the estimation of precipitable water over the oceans.

The radiative transfer formalism presented by Chang and Wilheit (1979) is adopted in this investigation. In this treatment the emissivity of the smooth sea surface has been calculated from the dielectric constant using the Fresnel relations (Jackson, 1962). The dielectric constant data of Lane and Saxton (1952) are used in these calculations. Inasmuch as the dielectric constant depends on the wavelength of the radiation and the temperature of the water, the microwave emissivity of the sea surface changes as a function of these variables.

In Figure 1 the emissivity, in the vertical and horizontal polarization of the smooth sea surface, calculated as a function of temperature, at different frequencies of SMMR is shown.

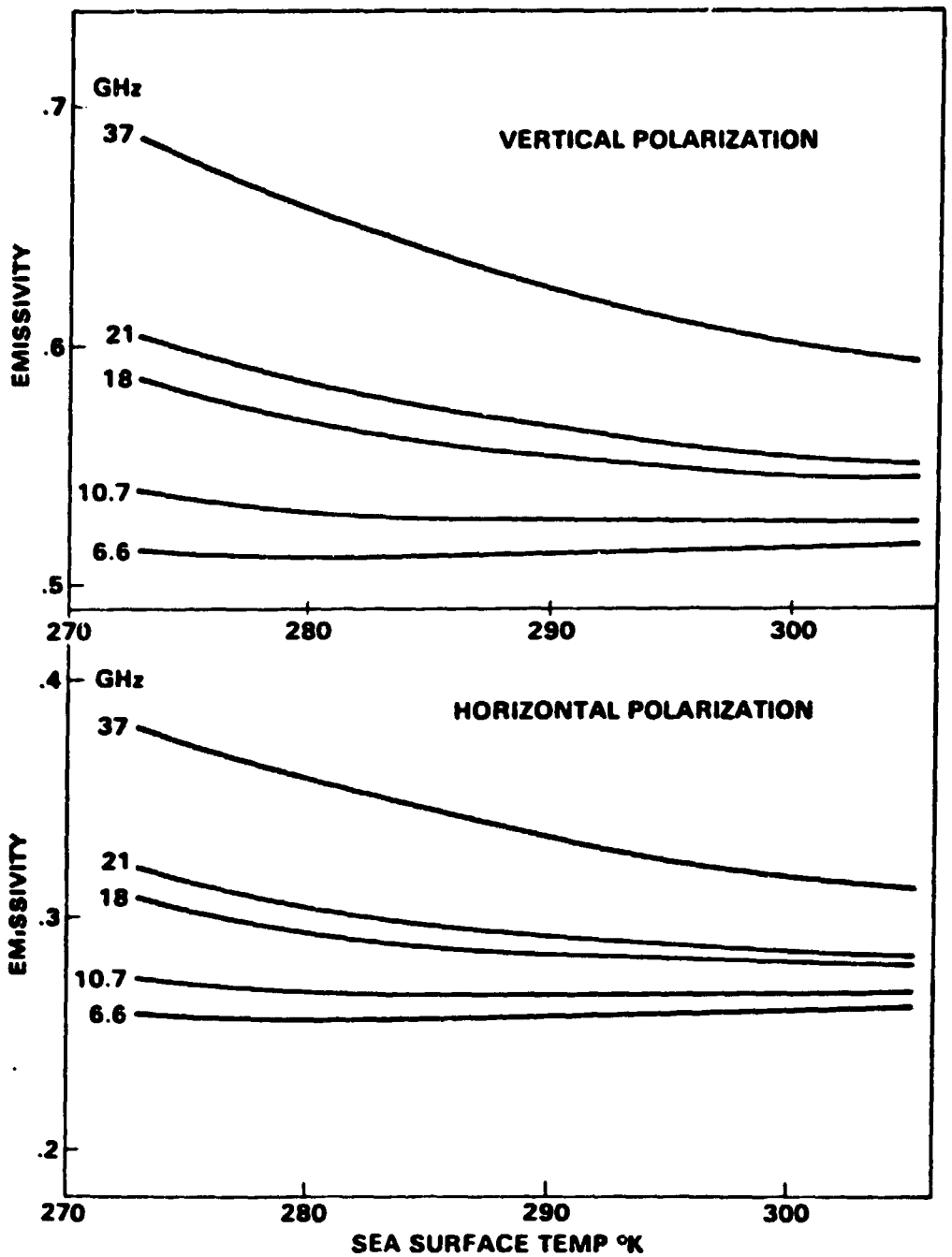

Figure 1. Variation of smooth sea surface emissivity as a function of temperature for SMMR frequencies.

The approach taken by Gaut (1968) for the absorption coefficient of water vapor is adopted. Weak absorption due to molecular oxygen in the atmosphere at frequencies below 45 GHz is also taken into account. The radiative transfer equation in the microwave region can be written as

$$T_{B_\nu} = T_0 \epsilon_\nu \tau_{0_\nu} + \int_{\tau_{0_\nu}}^{1} T(P)\, d\, \tau_\nu(P) + R_\nu \tau_{0_\nu} \int_{1}^{\tau_{0_\nu}} T(P)\, d\, \tau_\nu{}^{1}(P) \qquad (1)$$

where ν is the frequency

T_{B_ν} is the brightness temperature at the top of the atmosphere measured by the satellite sensor.

P is the pressure, T_0 and T(P) are the temperature at surface and at pressure level P, respectively;

τ_{0_ν} and $\tau_\nu(P)$ are the transmission of the atmosphere from the surface and from any pressure level P to the satellite respectively, along a direction 50° with respect to the local vertical.

ϵ_ν is the surface emissivity, R_ν is the reflectivity of the surface

Furthermore, $\epsilon_\nu + R_\nu = 1$

The first term in the transfer equation represents the surface emission, the second term the atmospheric emission, and the third term corresponds to the atmospheric radiation reflected at the surface and then transmitted to the satellite sensor. This last term is calculated assuming that the surface is rough on the scale of the microwave wavelengths and, furthermore, the surface acts like a Lambertian reflector.

Using Eq. (1), the brightness temperature spectrum between 6.6 GHz and 37 GHz, of the vertical polarized component of the radiation for a tropical atmosphere over the oceans with 3.42 $g/_{cm}{}^2$ of precipitable water is shown in Figure 2. This spectrum clearly reveals the shape of the weak water vapor line at 22.235 GHz. The spectral position of the various SMMR channels is shown. Shown in the same figure is a spectrum produced by the addition of a cloud between 1 and 2 km above the surface and containing 50 m $g/_{cm}{}^2$ of liquid water droplets (smaller than 100 μm in size). From this figure one can see that the brightness temperatures in all of the SMMR channels, 6.6, 10.7, 18, 21, and 37 GHz, are affected by the liquid water in clouds. In this case, the

absorption due to liquid water is weak at 18 and 21 GHz in comparison with that due to water vapor. Furthermore, the liquid water absorption increases by 36% (using the Rayleigh approximation) in going from 18 to 21 GHz, while the absorption due to water vapor increases by a factor of 4. Mainly because of this reason, as will be shown in more detail later, the difference in brightness temperature, $T_{21} - T_{18}$, remains approximately the same in the presence of a typical fair weather cloud containing less than 100 m $g/_{cm}{}^2$ of liquid water in a column (Stephens, 1978). In addition, by taking the difference $T_{21} - T_{18}$ we can practically eliminate the dependence on the surface temperature. This is illustrated in Figure 3 where the variation in brightness temperature T_{21} and T_{18} as a function of the surface temperature is shown. These brightness temperatures were computed by choosing one particular model atmosphere in which only the surface temperature was changed over a range of 20°C. The signal $T_{21} - T_{18}$ changes by only 0.6°C over this wide range of surface temperatures.

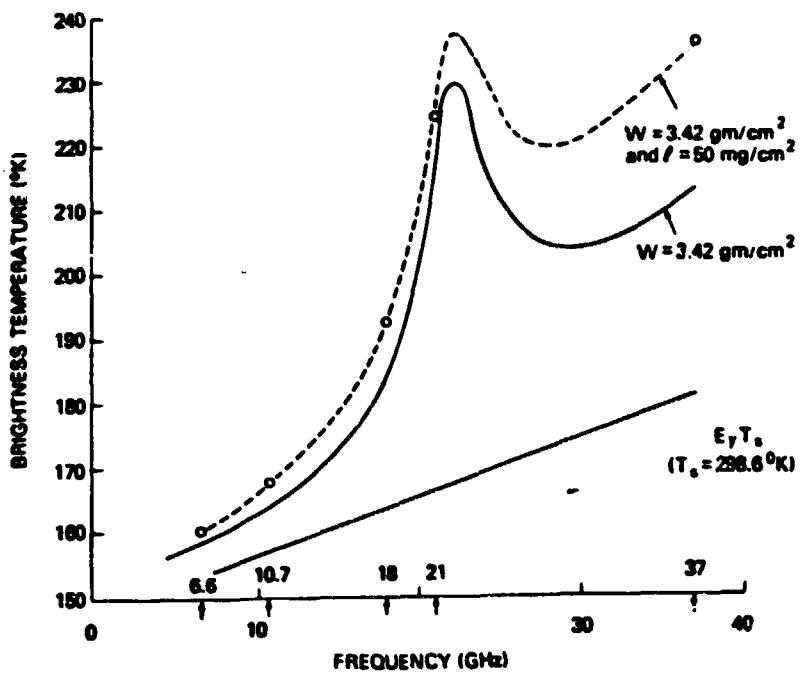

Figure 2. Brightness temperature spectra between 6 and 37 GHz for 1. No atmosphere (solid line); 2. A tropical model atmosphere with 3.42 g/cm^2 of precipitable water (solid curve); and 3. Addition of 50 m g/cm^2 of cloud liquid water to case 2 (dashed curve).

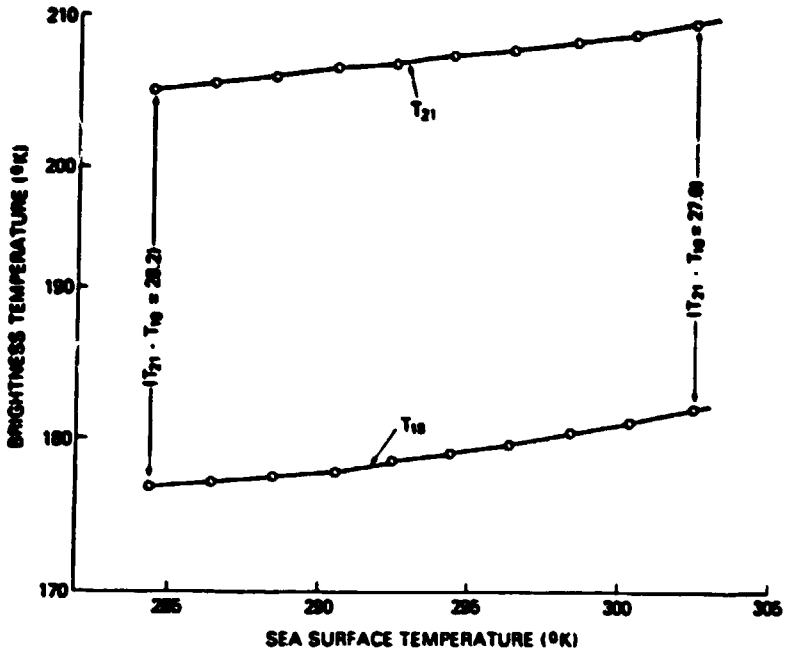

Figure 3. Brightness temperature variation at 18 and 21 GHz in the vertical polarization as a function of sea surface temperature, based on theoretical calculations.

On account of the reasons mentioned above and for its simplicity the signal $T_{21} - T_{18}$ is examined in detail for water vapor sensing. Wilheit and Chang (1980), in their multiple regression analysis, also find that the information contained in the brightness temperature measurements at 18 and 21 GHz is optimal for water vapor sensing. The reason for this is made clear in the following discussion.

With the radiative transfer equation we can express the brightness temperature difference $T_{21} - T_{18}$ as

$$(T_{21} - T_{18}) = T_o (\epsilon_{21} \tau_{o_{21}} - \epsilon_{18} \tau_{o_{18}}) + \int_{\tau_o}^{1} T(P)\, d[\tau_{21}(P) - \tau_{18}(P)]$$

$$+ \left[R_{21} \tau_{o_{21}} \int_{1}^{\tau_o} T(P)\, d\tau^{-1}_{21}(P) - R_{18} \tau_{o_{18}} \int_{1}^{\tau_o} T(P)\, d\tau^{-1}_{18}(P) \right] \qquad (2)$$

In this equation the first and the last terms depend upon the surface properties. When appropriate values of the parameters are introduced the terms have opposite sign and tend to cancel one another. The second term which represents the atmospheric emission thus makes the largest contribution to $T_{21} - T_{18}$. Since we are interested in obtaining the information on water vapor contained in the atmosphere this is a very desirable condition. In order to demonstrate this interesting behavior we have calculated the brightness temperatures, using detailed radiative transfer formalism, for 50 atmospheric cases ranging from high latitudes to the equator. These atmospheric cases correspond to radiosonde measurements made by ship stations. In Figure 4, calculations of $T_{21} - T_{18}$, are shown as a function of the precipitable water in the atmosphere, for both vertical and horizontal polarization. Also shown is the atmospheric emission term, which is common to both the vertical and horizontal polarizations. The atmospheric term lies between the curves for the two polarizations and accounts for a substantial part of $T_{21} - T_{18}$. The small scatter in the neighboring values of the atmospheric emission and $T_{21} - T_{18}$ in both polarizations shown in Figure 4 suggests that these quantities depend principally on the precipitable water and only in a secondary way on the sea surface temperature and vertical profiles of temperature and water vapor.

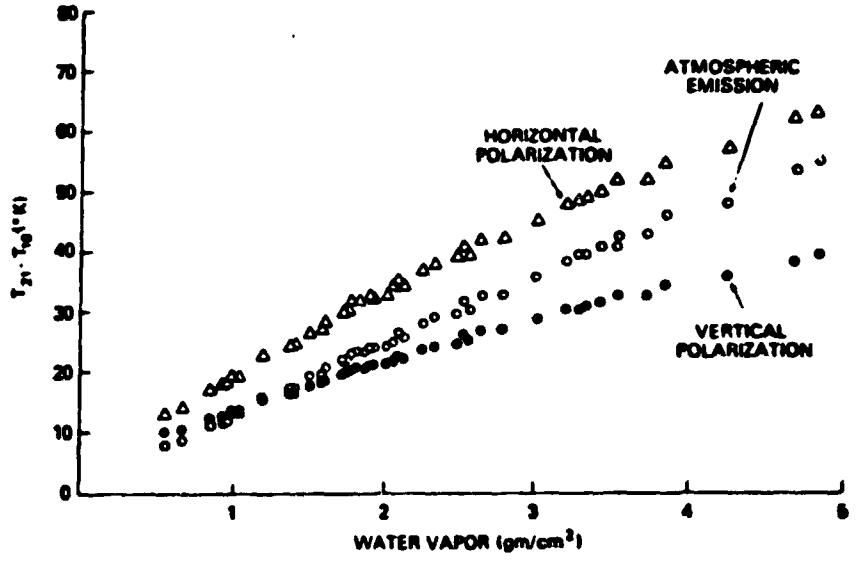

Figure 4. Theoretical relationship between $(T_{21} - T_{18})$, in the vertical and horizontal polarization, and precipitable water in the atmosphere. Atmospheric emission is calculated according to second term in equation (2) of the text.

At this point it is helpful to simplify equation (2) for the purposes of remote sensing. This can be done by approximating the integrals in the equation by choosing equivalent radiative temperature of the atmosphere. Further since the emissivity at 18 and 21 GHz differs only slightly (see Fig. 1) we can choose a mean emissivity $\tilde{\epsilon}$ for both the channels. With these approximations we get

$$(T_{21} - T_{18}) \cong \tilde{\epsilon}\, T_o\, (\tau_{o_{21}} - \tau_{o_{18}}) - \bar{T}\,(\tau_{o_{21}} - \tau_{o_{18}}) + (1 - \tilde{\epsilon})\, \bar{T}'\,(\tau_{o_{21}} - \tau_{o_{18}})\,[1 - (\tau_{o_{21}} + \tau_{o_{18}})] \qquad (3)$$

where $\bar{T}$ and $\bar{T}'$ are equivalent radiative temperatures of the upwelling and downwelling radiation. As the vertical distribution of water vapor is heavily weighted by the lower layers of the atmosphere we may approximate

$$T_o \cong \bar{T} \cong \bar{T}' \qquad (4)$$

Substituting the approximations (4) into equation (3) we get

$$(T_{21} - T_{18}) \cong \{(1 - \tilde{\epsilon})\, \bar{T}\,(\tau_{o_{21}} + \tau_{o_{18}})\}\ (\tau_{o_{18}} - \tau_{o_{21}}) \qquad (5)$$

(a) (b)

The quantity (a) on the right hand side of the equation remains nearly a constant, from equator to high latitudes (excluding sea ice), for realistic values of $\tilde{\epsilon}$ (see Fig. 1), τ_{18} and τ_{21} (see Fig. 5) and $\bar{T}$. The reason for this is $(1 - \tilde{\epsilon})\, \bar{T}$ decreases from equator to pole while $(\tau_{o_{21}} + \tau_{o_{18}})$ increases by about the same proportion.

This result suggests that one may seek a direct relationship between $T_{21} - T_{18}$ and the difference in the transmission, $\tau_{o_{18}} - \tau_{o_{21}}$, of the water vapor w in the atmosphere as follows:

$$T_{21} - T_{18} = C_0 + C_1\, e^{-k_{ox}\, mx}\, (e^{-k_{18} wx} - e^{-k_{21} wx}) \qquad (5)$$

where C_0 and C_1 are constnats to be determined from the theoretical calculations shown in Figure 4. K_{ox} is the effective absorption coefficient of oxygen at the central frequency of 19.5 GHz.

K_{18} and K_{21} are effective absorption coefficients for water vapor at 18 and 21 GHz, m is the path length of molecular oxygen in the atmosphere, x = Sec θ where $\theta = 50°$ corresponds to the viewing geometry of SMMR on Nimbus-7. These k values are determined from transmission computations made for the 50 ship radiosonde soundings that were mentioned earlier. The transmissions as a function of w for the 21 and 18 GHz are shown in Figure 5. The values of K_{18} and K_{21} estimated from Figure 5 are equal to 0.0116 and 0.0438 cm^2/gm respectively. A value of $e^{-k_{ox}mx} = 0.98$ is obtained from calculations. With these estimates we get the following equations to fit the calculated $T_{21} - T_{18}$ shown in Figure 4 for the horizontal and vertical polarizations.

$$(T_{21} - T_{18})_V = 5.7 + 169 \times .98 \, (e^{-k_{18}wx} - e^{-k_{21}wx}) \qquad (6)$$

$$(T_{21} - T_{18})_H = 6.1 + 289 \times .98 \, (e^{-k_{18}wx} - e^{-k_{21}wx}) \qquad (7)$$

Equations (6) and (7) fit the data shown in Figure 4 to within 1°K over the range of 0.5 to 5 $g/_{cm}^2$ of precipitable water.

From the Equations (6) and (7) one notices that the precipitable water signal $(T_{21} - T_{18})$ in the horizontal polarization is about 1.7 times larger than that in the vertical polarization essentially because of the difference in the surface emissivity for the two polarizations. One can take a linear combination of the two equations in an attempt to utilize the horizontal and vertical polarization measurements jointly.

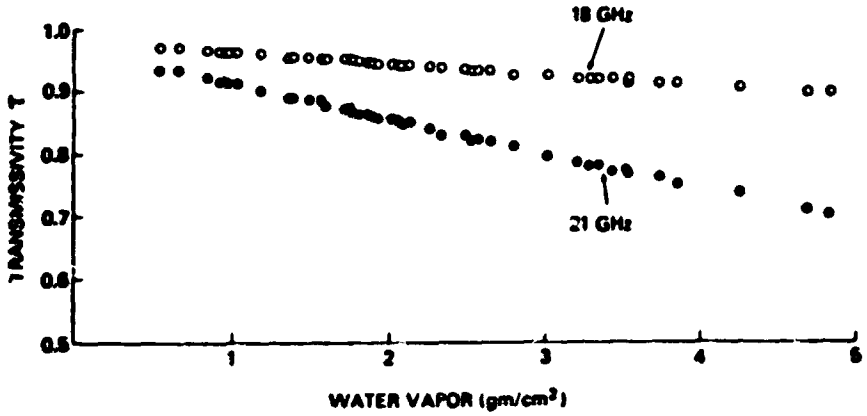

Figure 5. Transmissivity as a function of precipitable water in the atmosphere at 18 and 21 GHz.

Sources of Error in the Precipitable Water Estimation:

The rms error in the SMMR 18 and 21 GHz brightness temperature measurement, in a field of view of 156 km, is estimated to be 0.5°K (Gloersen et al., 1978). This will lead to an error of 0.7°K in $T_{21} - T_{18}$ which corresponds to an error of 0.1 $g/_{cm}^2$ of precipitable water. In order to estimate the error introduced by liquid water in the clouds we have calculated the brightness temperatures T_{21} and T_{18} for the set of 50 radiosonde profiles mentioned earlier, including liquid water clouds, containing 0, 25, and 50 m $g/_{cm}^2$ of the liquid distributed between 1 and 2 km above the surface. In Figure 6 the calculated $(T_{21} - T_{18})$ obtained from such calculations is shown as a function of the liquid water in the cloud. The isopleths of precipitable water, w, shown in the figure reveal the sensitivity of the estimated w to $(T_{21} - T_{18})$ in the presence of liquid water droplets. It is seen from the figure that below 2.7 $g/_{cm}^2$ W is overestimated in the presence of clouds. The opposite effect is seen above about 2.7 $g/_{cm}^2$. This error could be as large as 0.3 $g/_{cm}^2$ when the cloud liquid water content is 50 m $g/_{cm}^2$.

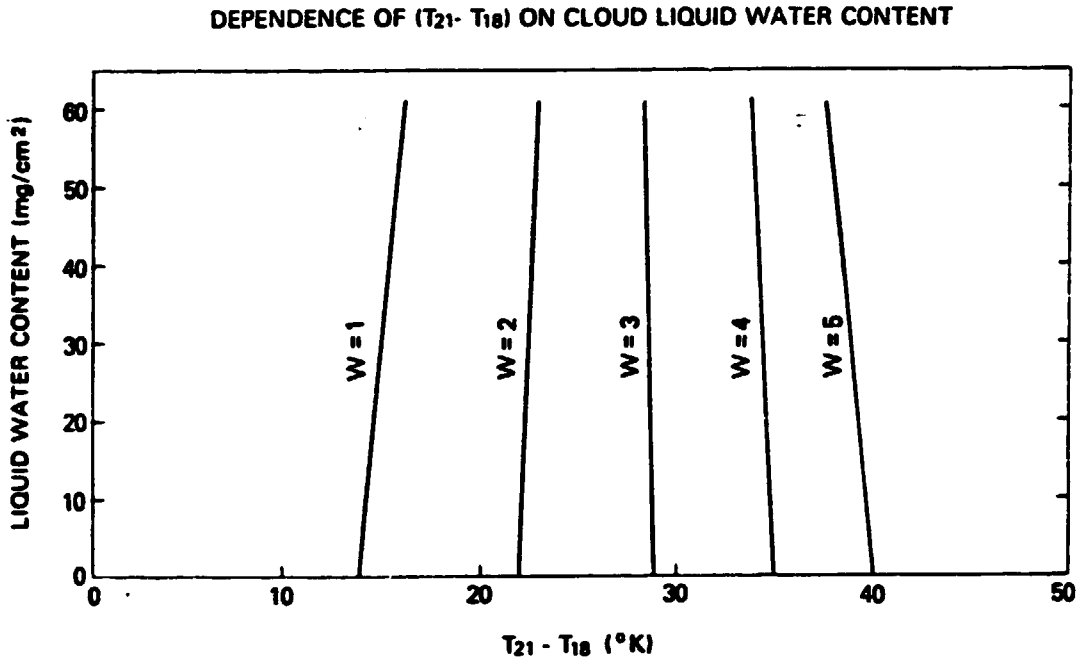

Figure 6. Variation of $(T_{21} - T_{18})$, in the vertical polarization, for a given precipitable water, in the presence of cloud liquid water content.

The winds at the surface increase the surface emissivity of the ocean and thus affect the satellite measured brightness temperatures. Taking Wilheit's (1979) model of the surface brightness change produced by wind at different wavelengths, we find that ($T_{21} - T_{18}$) will be systematically reduced by the surface winds. This results in a systematic underestimation of precipitable water. A surface wind of 30 m/sec results in an underestimation of precipitable water by about 10%. Further, this effect is almost linearly proportional to the wind speed.

From the discussion of these errors we see that the error introduced by substantial liquid water in the clouds and high winds could be appreciable. However, the errors introduced under average conditions of wind (10 m/sec) and clouds (assumed to contain less than 30 m $g/_{cm}^2$) should lead to an error of about 0.2 $g/_{cm}^2$. Now if we consider all the sources of error, (instrument noise, surface winds and clouds) one can expect an error of about 0.3 $g/_{cm}^2$.

Comparison with radiosonde measurements:

For the purposes of comparison an independent sample of 28 coincident ship radiosonde measurements and Nimbus-7 SMMR observations were obtained. Coincidence is assumed when the center of the satellite field of view is within 1° latitude and longitude of the ship location and when the time difference between the ship and the satellite observations does not exceed one day. The satellite data used in this study have a foot print size of 156 km. The Nimbus-7 SMMR data have some systematic calibration bias. We find the bias in the vertical polarization measurements to be considerably smaller than that in the horizontal polarization. In order to assess this systematic bias the brightness temperatures are calculated at the SMMR frequencies utilizing the detailed radiative transfer formalism described earlier. Ship-radiosonde measured temperature, and water vapor profiles are used in these radiative transfer calculations. Winds at the surface and liquid water in the cloud, if any, are not considered. When ($T_{21} - T_{18}$) computed in this fashion is compared with that observed by SMMR it is found that the satellite measurements yield a value that is large systematically by 8.5°K. After removing this bias, precipitable water

is estimated from SMMR data with the help of Equation (6). In Table 1 the relevant data observed from the satellites and ship radiosonde measurements is presented.

In Figure 7 these estimates of w from SMMR are compared with those of radiosondes. The agreement between the two sets of data is good yielding an rms error of 0.25 $g/_{cm}{}^2$. This error is not inconsistent with the error analysis presented in the previous section. Wilheit and Chang (1980) developed a multiple regression relationship between the precipitable water in the atmosphere and the brightness temperatures in the vertical and horizontal polarizations at 18 and 21 GHz. A test of their method with the present sample of radiosonde data yields an rms error in the precipitable water of 0.3 $g/_{cm}{}^2$ which is not significantly larger than the value obtained in the present study. Inclusion of horizontal polarization components, which are more susceptable to variability of sea surface state, in Wilheit and Chang's regression technique could result in slightly larger errors.

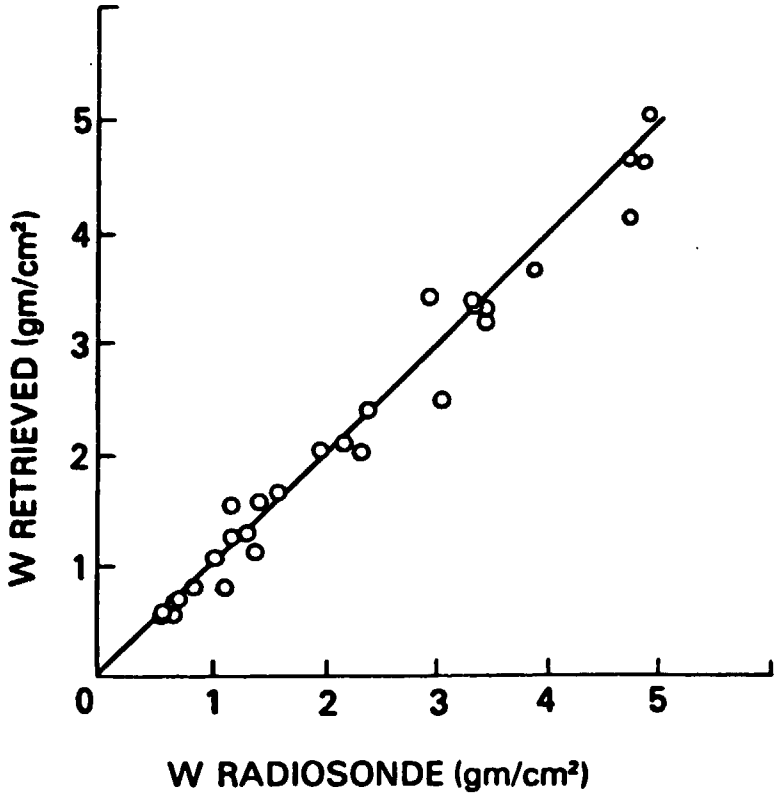

Figure 7. Comparison of ship radiosonde measured precipitable water with that estimated from Nimbus-7 SMMR data.

The regression method of Grody et al. (1980) based on the measurements of Scanning Microwave Spectrometer (SCAMS) on Nimbus-6 at 22 and 31 GHz yielded an error of about $0.45 g/cm^2$. This somewhat larger error is attributed to the use of different spectral measurements in their investigation.

Global maps of precipitable water:

Utilizing the Nimbus-7 SMMR measurements for a period of two months: Oct. 25 - Nov. 25, 1978, and Feb. 15 - Mar. 17, 1979, we have derived global maps of precipitable water on a weekly basis (see Figures 8 - 15). The $(T_{21} - T_{18})_v$ observed by SMMR in the vertical polarization is used for this purpose. Two monthly mean global maps, one for Oct. 25 - Nov. 25, 1978, and another for Feb. 15 - Mar. 17, 1979, are also generated (Figures 16 and 17).

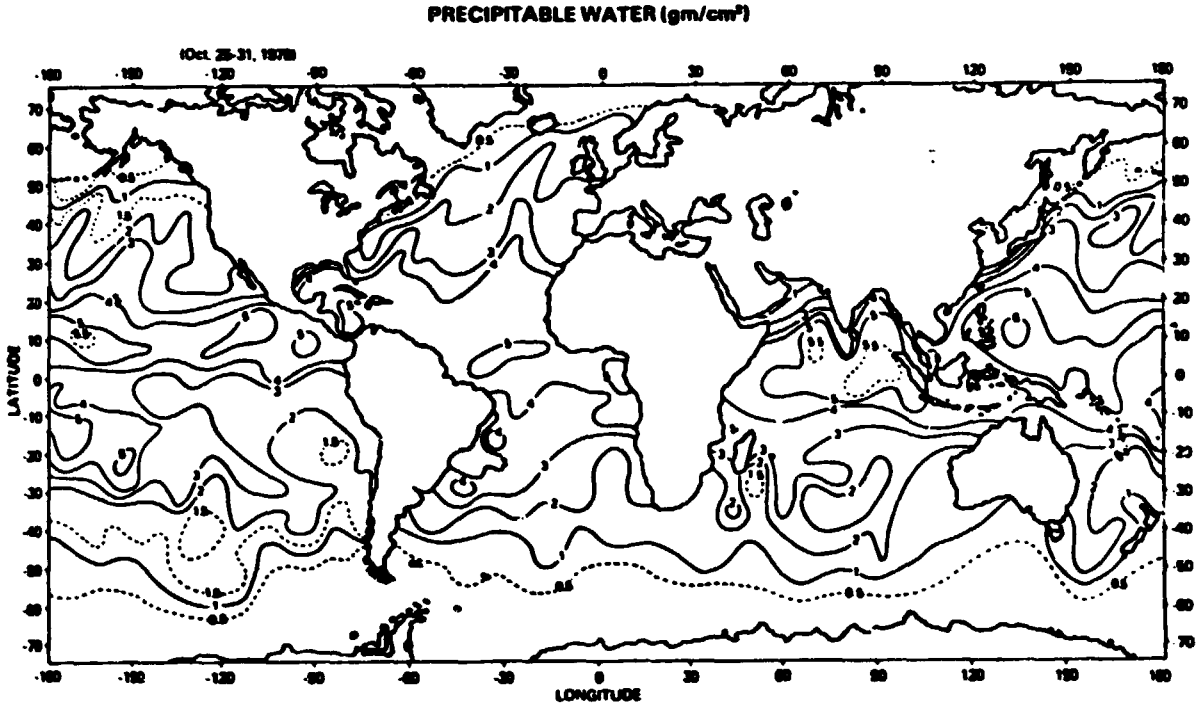

Figure 8. Distribution of precipitable water in the atmosphere, over the global oceans, derived from Nimbus-7 SMMR data for the period Oct. 25 - 31, 1978.

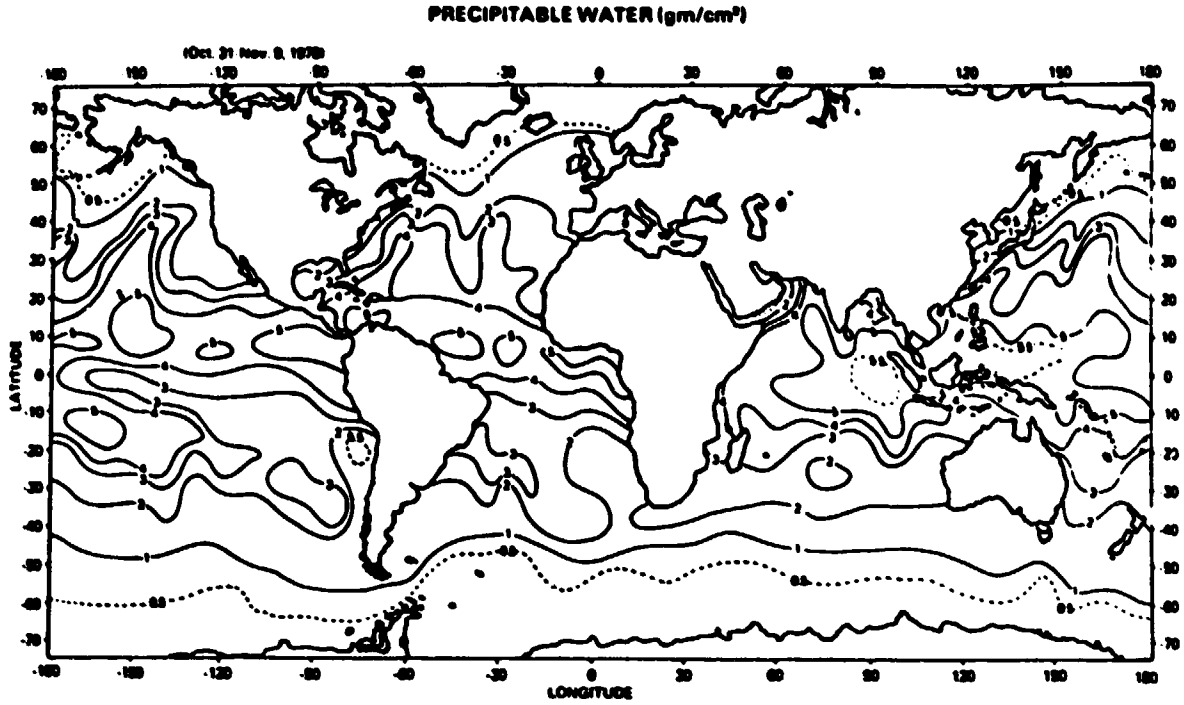

Figure 9. Distribution of precipitable water in the atmosphere, over the global oceans, derived from Nimbus-7 SMMR data for the period Oct. 31 - Nov. 9, 1978.

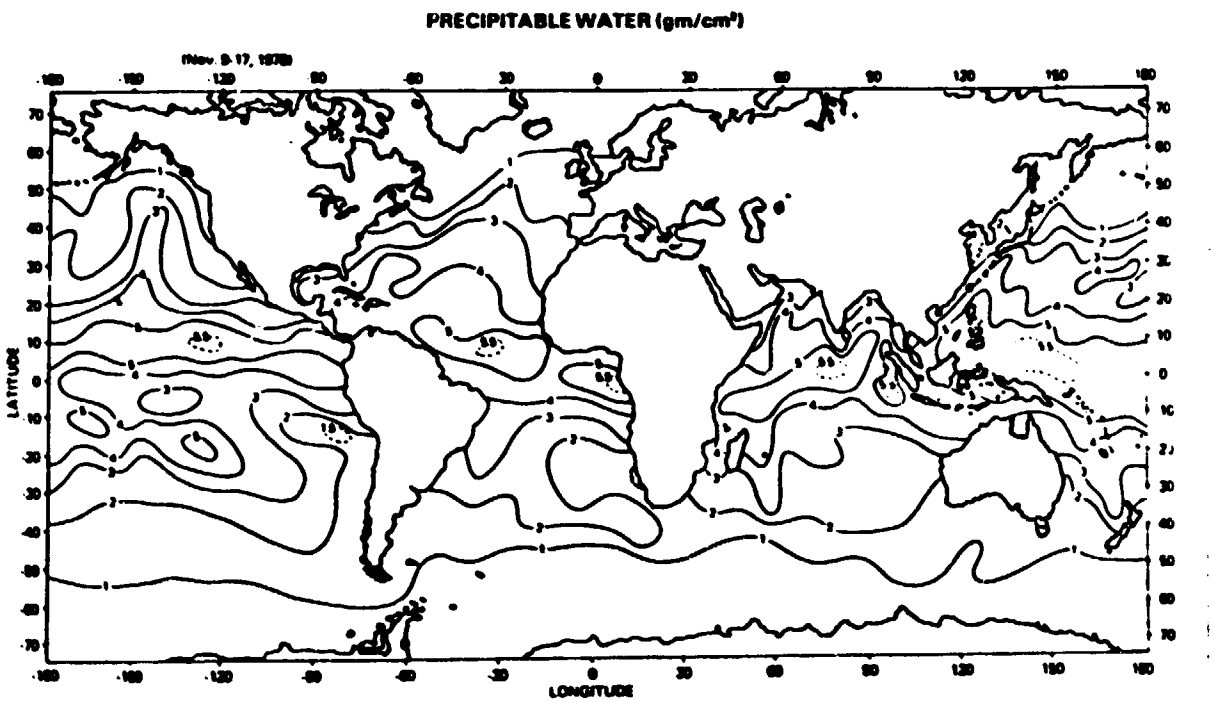

Figure 10. Distribution of precipitable water in the atmosphere, over the global oceans, derived from Nimbus-7 SMMR data for the period Nov. 9 - 17, 1978.

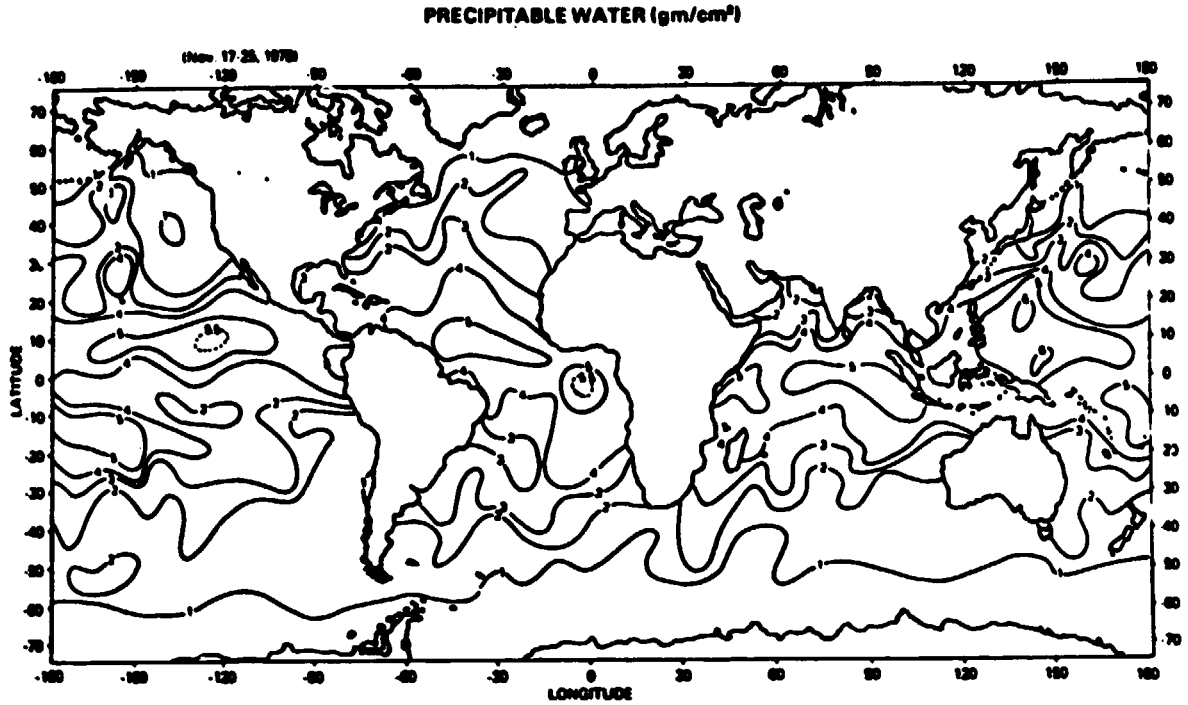

Figure 11. Distribution of precipitable water in the atmosphere, over the global oceans, derived from Nimbus-7 SMMR data for the period Nov. 17 - 25, 1978.

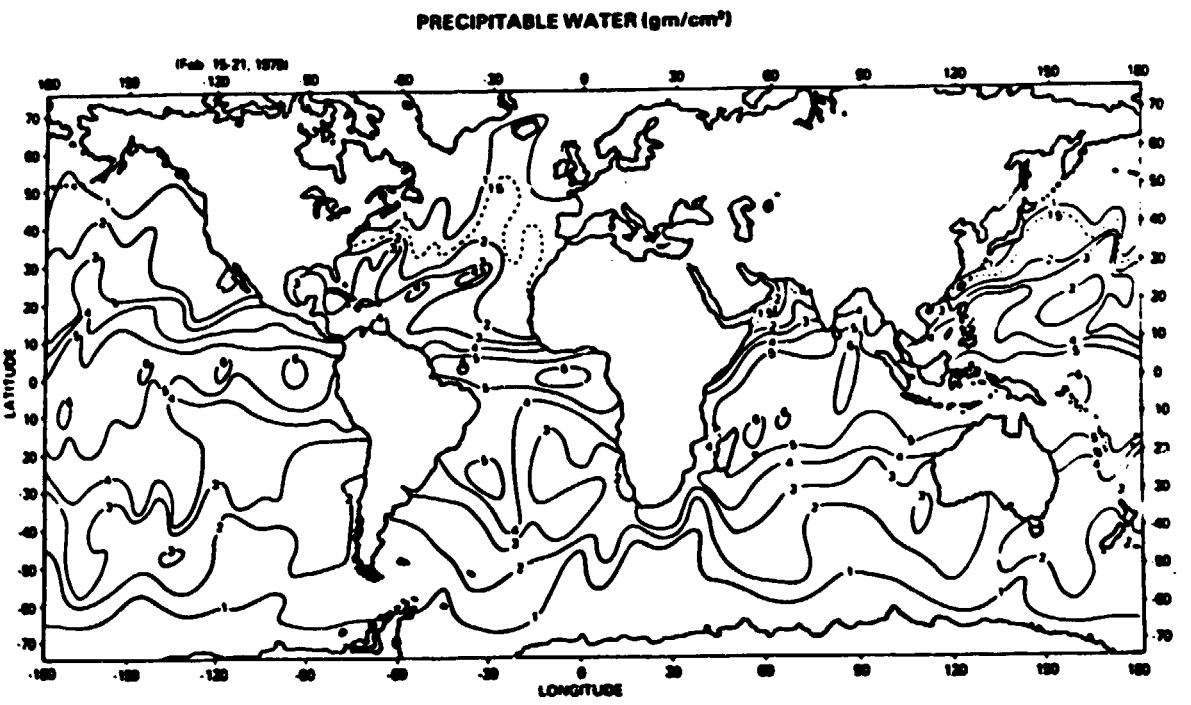

Figure 12. Distribution of precipitable water in the atmosphere, over the global oceans, derived from Nimbus-7 SMMR data for the period Feb. 15 - 21, 1979.

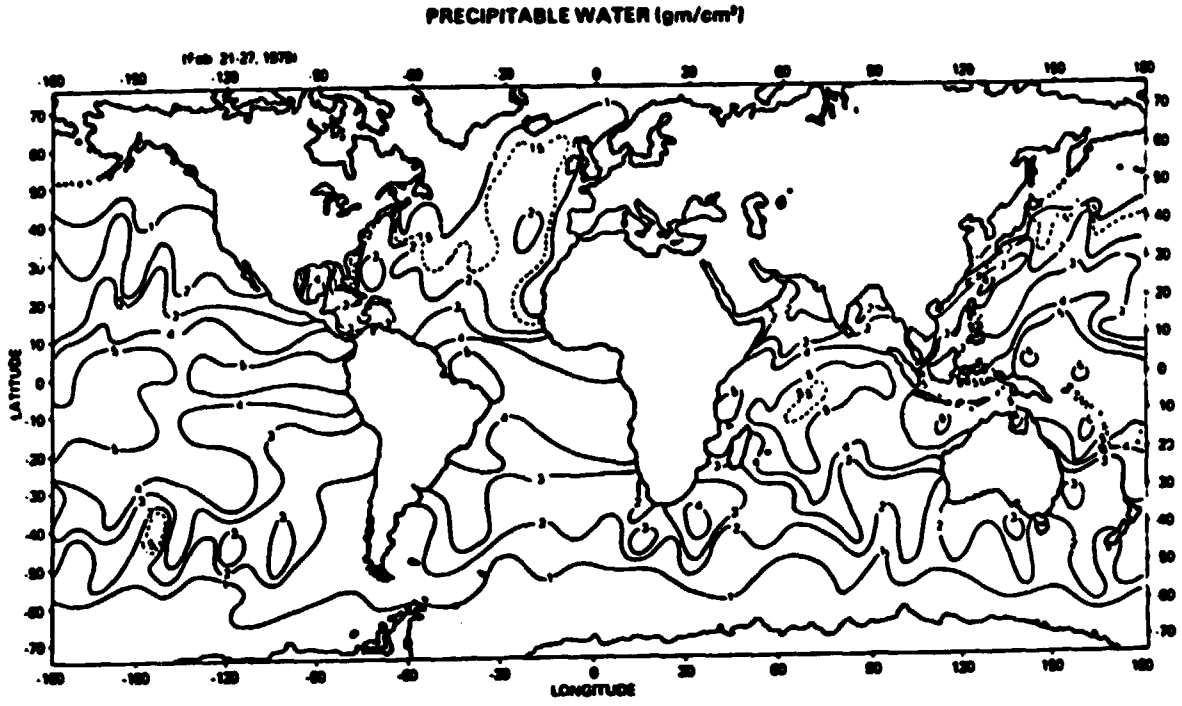

Figure 14. Distribution of precipitable water in the atmosphere, over the global oceans, derived from Nimbus-7 SMMR data for the period Feb. 21 - 27, 1979.

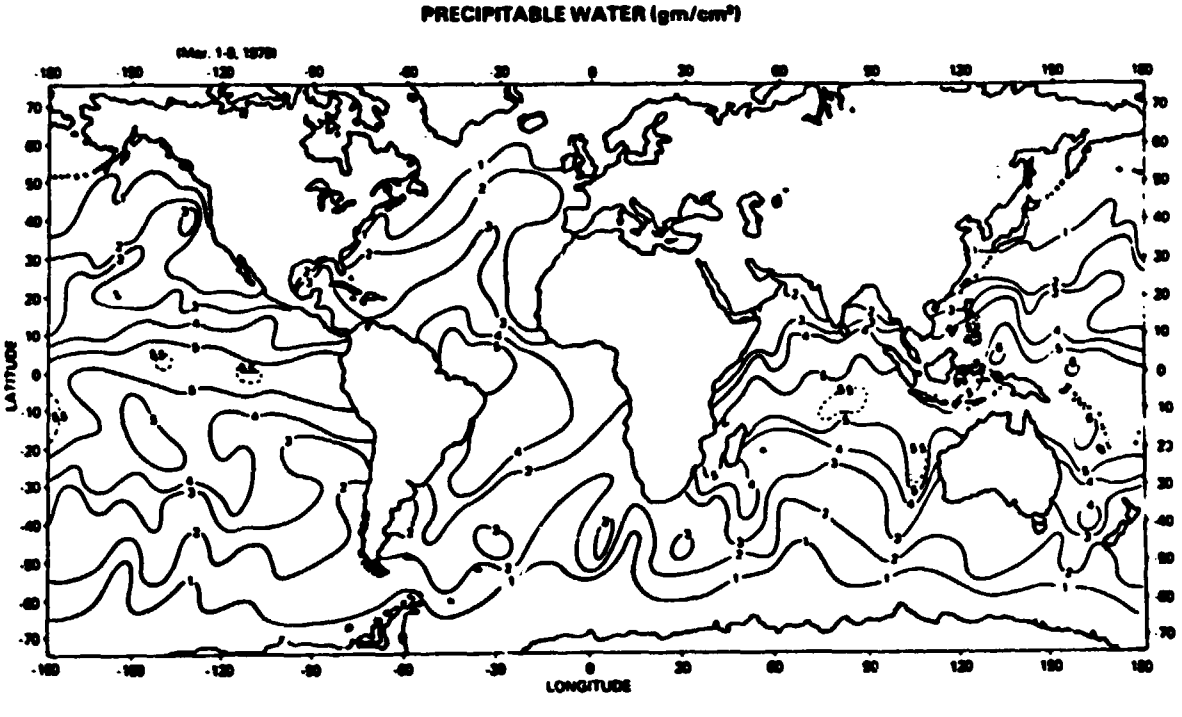

Figure 15. Distribution of precipitable water in the atmosphere, over the global oceans, derived from Nimbus-7 SMMR data for the period Mar. 1 - 9, 1979.

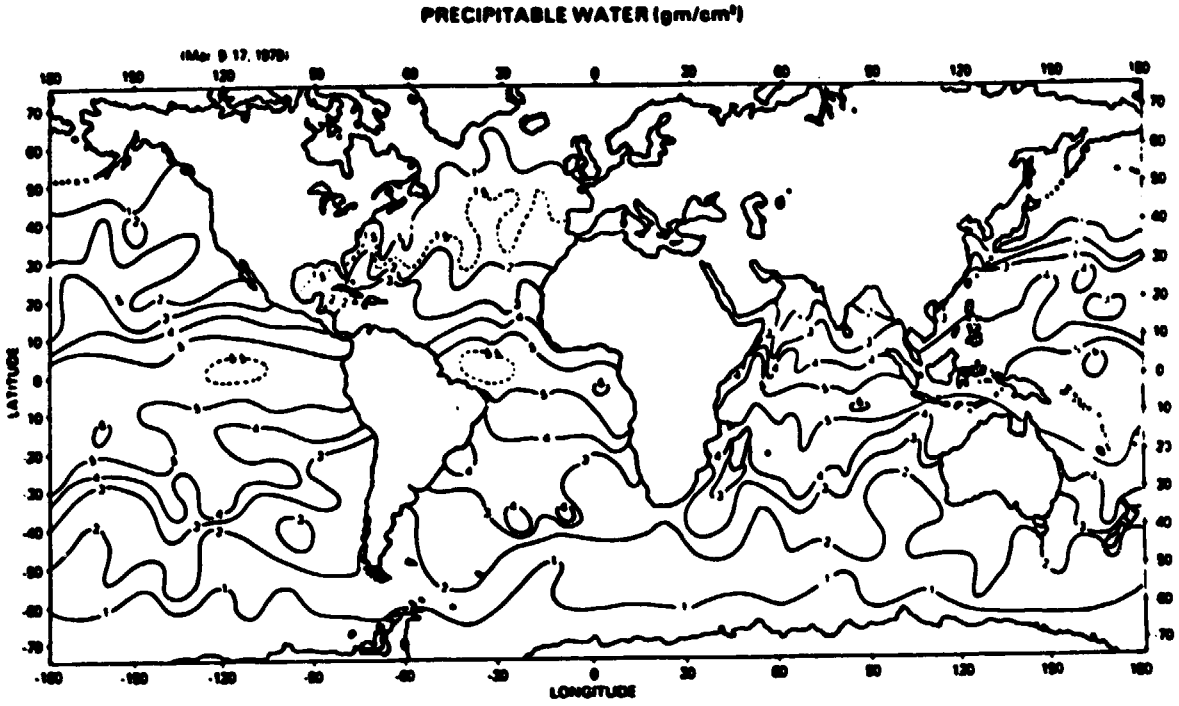

Figure 15. Distribution of precipitable water in the atmosphere, over the global oceans, derived from Nimbus-7 SMMR data for the period Mar. 9 - 17, 1979.

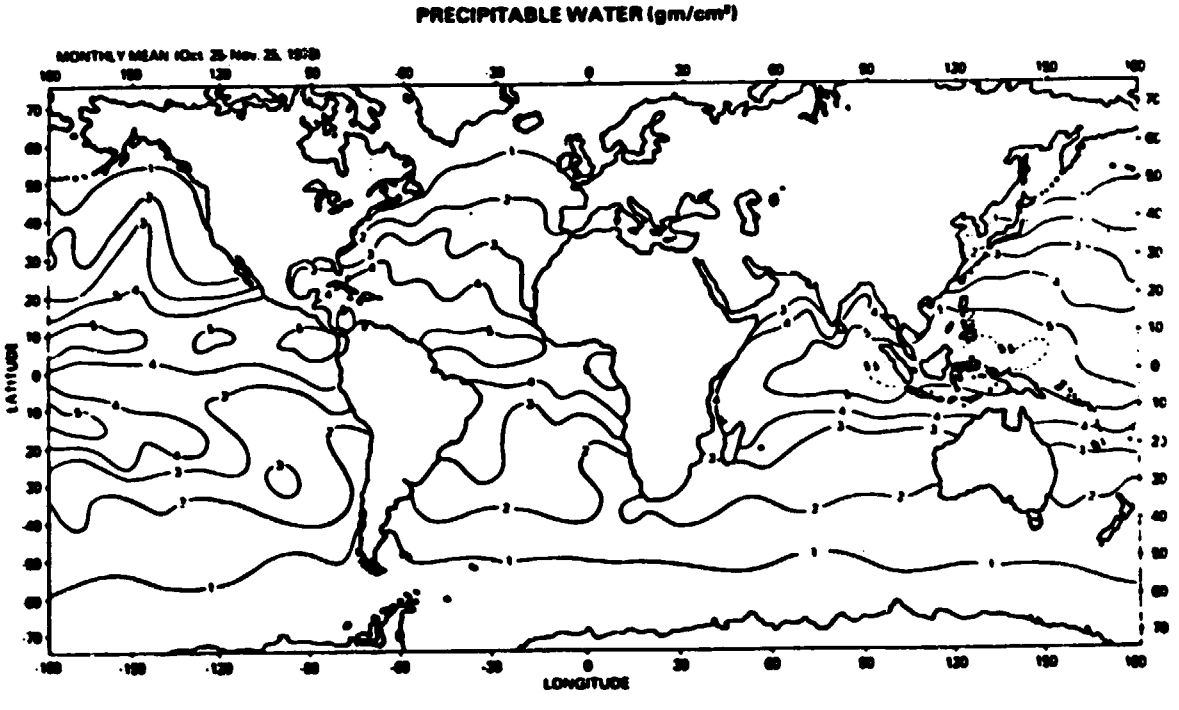

Figure 16. Distribution of precipitable water in the atmosphere, over the global oceans, derived from Nimbus-7 SMMR data for the period of Oct. 25 - Nov. 25, 1978.

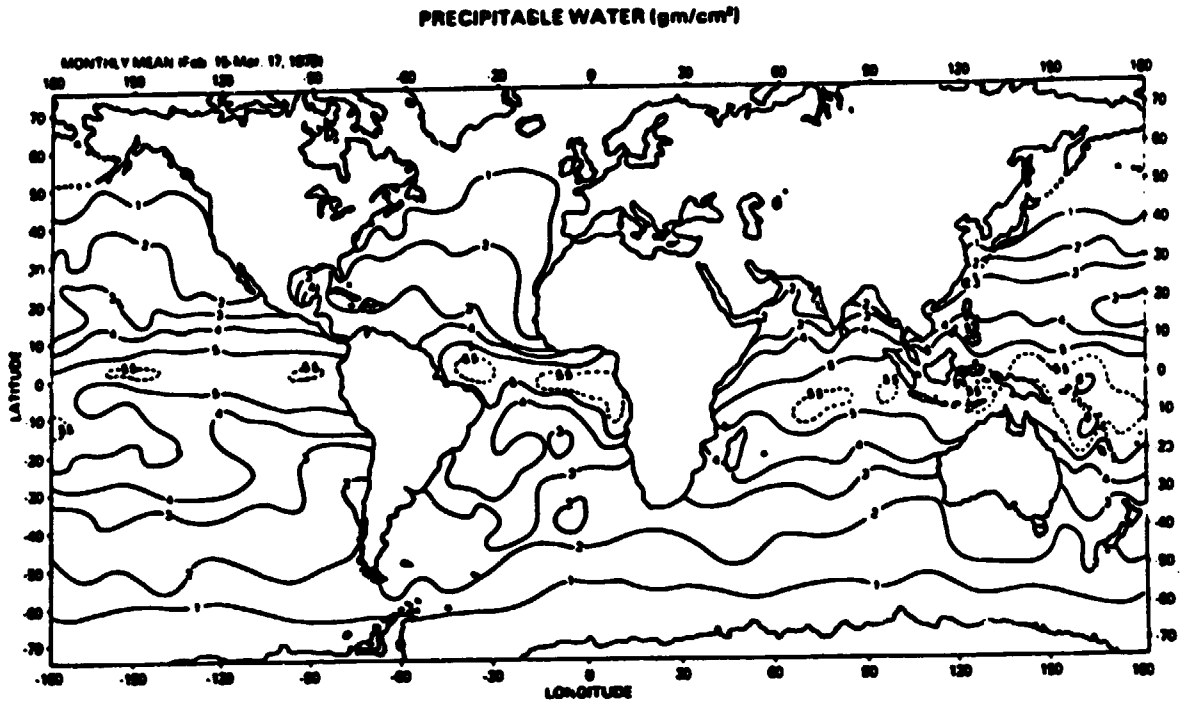

Figure 17. Distribution of precipitable water in the atmosphere, over the global oceans, derived from Nimbus-7 SMMR data for the period of Feb. 15 - Mar. 17, 1979.

The SMMR data have enabled us to use a field of view of 156 km which is significantly better than the 250 km field of view of the Nimbus 6 NEMS used in the earlier microwave water vapor sensing studies (Grody, 1977, and Grody, et al., 1980). Also the rms error of the present method is ~ 0.25 g/cm^2 compared to ~ 0.45 g/cm^2 of the earlier microwave methods. On account of these reasons we are able to obtain finer information on the global distribution of precipitable water.

An examination of the maps of precipitable water reveals minima in the eastern parts of subtropical Atlantic and Pacific oceans in the northern and southern hemispheres. These are regions of large scale subsidence. The relatively dry tongue associated with the subsidence motion (Bjerknes, 1969) in the eastern equatorial Pacific is clearly revealed. The maxima of precipitable water associated with the Intertropical Convergence Zone (ITCZ) can be noticed both to the north and

south of the equator. The progressive movement of ITCZ can be followed from these maps. Most of these characteristics were revealed in the earlier studies using the microwave and infrared satellite data.

Because of the improved spatial resolution and accuracy we are able to derive some finer information in the present analysis. The isopleths of the precipitable water show a marked orientation along the direction of flow of warm ocean currents such as the Gulf Stream and Kuroshio. The gradient of precipitable water is in a direction normal to such warm ocean currents, suggesting an increase in precipitable water accompanies an increase in the sea surface temperature. This is observed generally on the east coast of the continents. Similarly the influence of the cold ocean currents, such as the California current and the Peruvian current, on the west coast of the continents can be appreciated.

Water vapor maps are also useful in some synoptic studies. Particularly the influence of the cold air outbreak over the warm waters can be examined. An episode of cold air outbreak, that took place off of the northeast U.S.A. onto Atlantic Ocean, during Feb. 1979 is examined here. The global water vapor map of the Feb. 15 to 21, 1979, shows the distribution of the precipitable water to the east of U.S.A. when there was a cold air outbreak onto the warm waters of Gulfstream. The map for the following week, shows the modified distribution of precipitable water after the cold air outbreak had subsided. The change in the precipitable water between the two weekly maps is shown in Fig. 18 which reveals striking increase in w adjacent to the north east U.S. This implies that cold air flow had advected away from the coastal waters significant amount of water vapor. This in turn means significant amount of latent heat is transferred from the ocean surface to the atmosphere. This follows from the following reasoning. Let us consider the conservation equation for water vapor.

$$\frac{\partial w}{\partial t} + \mathbf{V} \cdot \nabla_H w + w \nabla_H \cdot \mathbf{V} = \text{EVAPORATION} - \text{PRECIPITATION} \qquad (6)$$

where w is the precipitable water, bulk of which is contained in the boundary layer.

$\mathbb{V}$ is the mean wind in the boundary layer

$\nabla_H w$ is the horizontal gradient of w

$\nabla_H \cdot \mathbb{V}$ is the horizontal divergence of mean wind

Now if we neglect $\nabla_H \cdot \mathbb{V}$ and precipitation in the vicinity of N.E./U.S. when the cold air was blowing strongly and assume a quasi steady state, during cold air outbreak we get

$$\mathbb{V} \cdot \nabla_H \; w = \text{EVAPORATION} \qquad (7)$$

This permits us to estimate the evaporation or the latent heat input into the atmosphere if we have wind information together with the horizontal gradient of w.

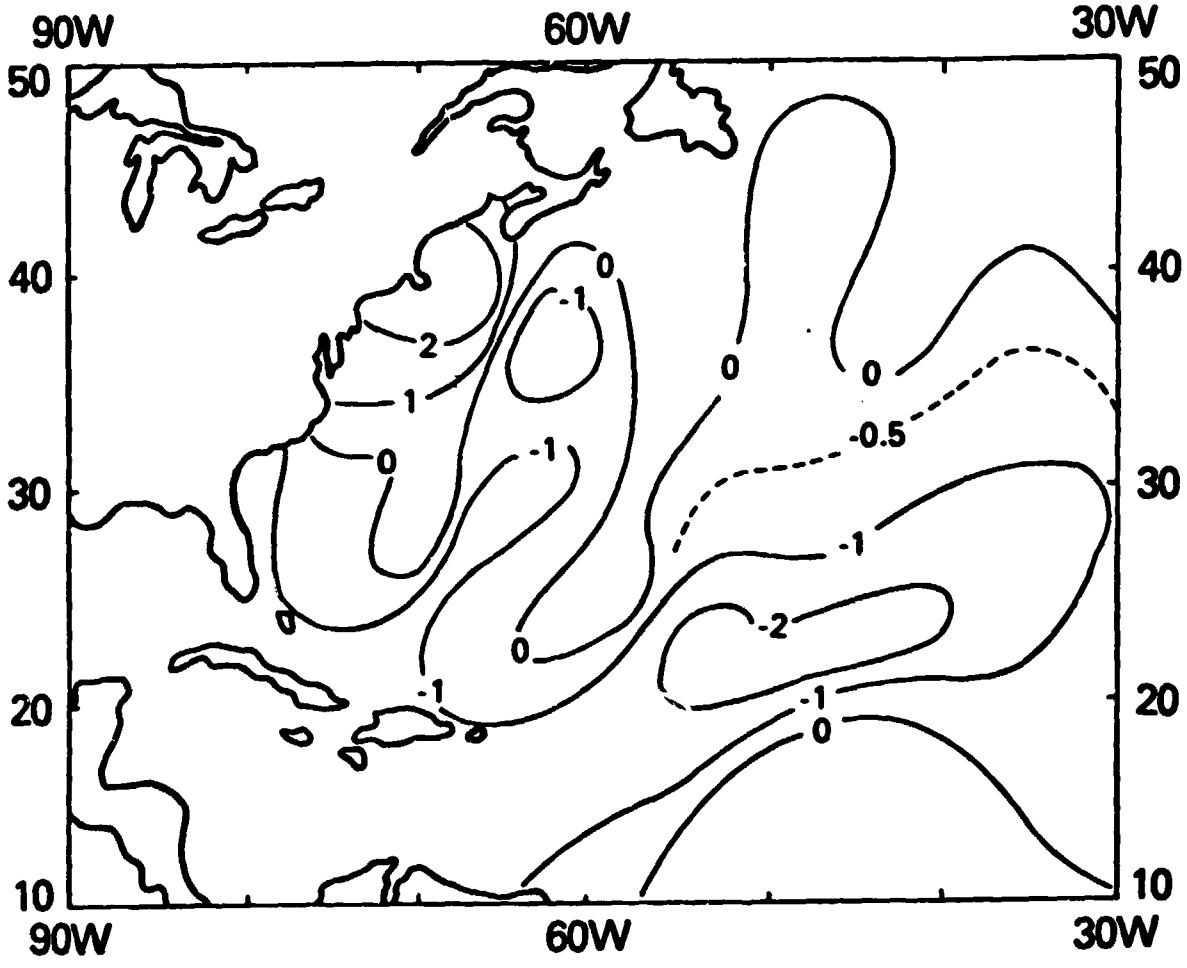

Figure 18. Change in precipitable water (g/cm^2) from the week of Feb. 21 - 27, 1979.

It is possible to get the wind speed and precipitation information from SMMR data (Wilheit, 1978). The wind velocity could be obtained from microwave scatterometer data (Halberstam, 1980). Thus it appears that one can attempt to estimate over the global oceans fluxes of latent heat input into the atmosphere from microwave measurements using equation (6).

Conclusions:

Nimbus-7 SMMR microwave brightness temperature measurements in the 18 and 21 GHz channels are found to be very useful for remote sensing of precipitable water in the atmosphere over the oceans. The signal obtained by taking the difference between the measured brightness temperature in two channels, $T_{21} - T_{18}$, greatly reduces the noise introduced by the variations in surface temperature, and the atmospheric profiles of the temperature and water vapor. Non-raining clouds containing liquid water droplets amounting to less than 30 m $g/_{cm}{}^2$ and light winds at the surface, less than 10 m/s, constitute a source of error of about 0.3 $g/_{cm}{}^2$. However, heavy winds and clouds containing substantial amounts of liquid water can introduce substantial error. With the exception of the surface winds, the infrared remote sensing methods to estimate precipitable water in the atmosphere depend sensitively on the sea surface temperature, temperature and water vapor profiles, and clouds of all kinds. Incorrect specification of these variables can lead to significant errors in the infrared methods. Thus, considering the merits of the infrared and microwave remote sensing techniques to retrieve precipitable water in the atmosphere, over the oceans, it appears that the microwave approach is preferable for both accuracy and spatial coverage. As the precipitable water is a good tracer of the dynamics of lowest layers in the atmosphere over the oceans, these microwave measurements will be valuable for weather and climate studies.

ACKNOWLEDGEMENTS

We are thankful to Dr. T. T. Wilheit for his suggestions and comments which have enabled us to improve this paper.

REFERENCES

Bjerknes, J., 1969, "Atmospheric teleconnections from the equatorial Pacific" Monthly Weather Review, Vol 97, pp. 163 - 172.

Chang, A. T. C. and T. T. Wilheit (1979), Remote sensing of atmospheric water vapor, liquid water, and wind speed at the ocean surface by passive microwave techniques from Nimbus 5 satellite. Radio Science, Vol 14, pp 793 - 803.

Conrath, B. J. (1969), On the estimation of relative humidity profiles from medium resolution infrared spectra obtained from a satellite. Jour of Geoph., Res. Vol 74, pp. 3347 - 3361.

Gaut, N. E., (1968), "Studies of Atmospheric water vapor by means of passive microwave techniques." Tech. Rep. 467, Res. Lab. of Elec., Mass. Inst. of Technol., Cambridge.

Gloerson, P. and L. Hardis, (1978) "Scanning Multichannel Microwave Radiometer (SMMR) Experiment" Nimbus 7 Users' Guide, NASA, Goddard Space Flight Center, Greenbelt, Md. Edited by C. R. Madrid.

Grody, N. C., (1968), High resolution passive microwave satellite, applications to synoptic meteorology and climatology. Application Review Panel Report. D. H. Staelin and P. W. Rosenkranz editors, MIT Research Laboratory of Electronics, 6. 1-6.40.

Grody, N. C., A. Gruber and W. C. Shen, (1980), Atmospheric Water content over Tropical Pacific derived from Nimbus 6 Scanning Microwave Spectrometer, Jour. of Applied Meteorology, Vol. 19, pp. 986 - 996.

Gunn, L. L. S. and T. W. R. East, (1954), The microwave properties of precipitation particles Quart. Jour. of Roy. Met. Soc., Vol. 80, pp. 522 - 545.

Helberstam, I., (1980), Some consideration in the evaluation of Seasat-A-Scatterometer (SASS) Measurements Jour. of Physical Oceanography, Vol. 10, pp 623 - 632.

Jackson, J. D. (1962), Classical Electrodynamics, Page 219. John Wiley, New York.

Lane, J. A. and J. A. Sexton, (1952), Electrical properties of Sea Water, Wireless Engineering, Vol. 29, pp. 269 - 275.

Prabhakara, C., G. Dalu, R. C. Lo and N. R. Nath, (1979), Remote sensing of seasonal distribution of precipitable water vapor over the oceans and the inference of boundary layer structure, Monthly Weather Review, Vol. 107, pp. 1388 - 1401.

Plass, G. N., (1960), Useful representations for measurements of spectral band absorption. J. Opt. Soc. Am. Vol. 50, p. 868.

Smith, W. L. and H. M. Woolf, (1976), The use of eignenvectors of statistical covariance matrices for interpreting satellite sounding radiometer observations. Jour. of Atm. Sc. Vol. 33, pp. 1127 - 1140.

Staelin, D. H., K. F. Kumzi, R. L. Pettyjohn, R. K. L. Poon, R. W. Wilcox and J. W. Waters, (1976), Remote sensing of atmospheric water vapor and liquid with the Nimbus 5 microwave spectrometer, Jour. of Applied Meteorology, Vol. 15, pp. 1204 - 1214.

Stephens, G. L., (1978), Radiation profiles in extended water clouds. I: Theory, Jour. of Atm. Sc., Vol. 35, pp 2111 - 2122.

Wilheit, T. T., M. S. V. Rao, T. C. Chang, E. B. Rodgers, J. S. Theon, (1977), A satellite technique for quantitative mapping rainfall rates over the oceans. Jour. of Applied Meteorology, Vol. 15, pp. 1204 - 1214.

Wilheit, T. T., (1978), A review of applications of microwave radiometry to oceanography, Boundary Layer Meteorology, Vol. 13, pp. 277, 293.

Wilheit, T. T. (1979), "A model for the microwave emissivity of the oceans' surface as a function of wind speed". IEE Transactions on Geoscience Electronics, Vol. GE -17, pp. 244 - 249.

Wilheit, T. T. and A. T. C. Chang, (1980), An algorithm for retrieval of ocean surface and atmospheric parameters from the observations of the Scanning Multichannel Microwave Radiometer (SMMR). Radio Science, 15 525-544 (1980).